

Journal of Materials Chemistry A

Accepted Manuscript



This is an *Accepted Manuscript*, which has been through the Royal Society of Chemistry peer review process and has been accepted for publication.

Accepted Manuscripts are published online shortly after acceptance, before technical editing, formatting and proof reading. Using this free service, authors can make their results available to the community, in citable form, before we publish the edited article. We will replace this *Accepted Manuscript* with the edited and formatted *Advance Article* as soon as it is available.

You can find more information about *Accepted Manuscripts* in the [Information for Authors](#).

Please note that technical editing may introduce minor changes to the text and/or graphics, which may alter content. The journal's standard [Terms & Conditions](#) and the [Ethical guidelines](#) still apply. In no event shall the Royal Society of Chemistry be held responsible for any errors or omissions in this *Accepted Manuscript* or any consequences arising from the use of any information it contains.

Cite this: DOI: 10.1039/c0xx00000x

www.rsc.org/xxxxxx

ARTICLE TYPE

High performance nano sheet-like silicoaluminophosphate molecular sieves: synthesis, 3D EDT structural analysis and MTO catalytic studies

Qiming Sun,^{a*} Yanhang Ma,^{b*} Ning Wang,^a Xu Li,^a Dongyang Xi,^a Jun Xu,^c Feng Deng,^c Kyung Byung Yoon,^d Peter Oleynikov,^b Osamu Terasaki,^{e,f} and Jihong Yu^{*a}

Received (in XXX, XXX) Xth XXXXXXXXX 20XX, Accepted Xth XXXXXXXXX 20XX

DOI: 10.1039/b000000x

Nano sheet-like silicoaluminophosphate (SAPO) molecular sieves SAPO-34 (CHA-type) and SAPO-18 (AEI-type) with different silicon contents were synthesized under hydrothermal conditions by using tetraethylammonium hydroxide as the template. Three-dimensional electron diffraction tomography (3D EDT) technique was applied for *ab initio* structure solutions. Electron microscopy observations certified the existence of defects, i.e., intergrowth of CHA- and AEI-type frameworks caused by different stacking manners of double 6-ring layers, but the layers were highly coherent along *c* direction. Compositions, acidities, chemical environments, and texture properties of all samples were characterized by ICP, EDS, NH₃-TPD, MAS NMR, and N₂ adsorption/desorption measurements. The catalytic performances of methanol-to-olefin (MTO) reactions over nano SAPO catalysts with different silicon contents were systematically studied. All of these catalysts showed excellent catalytic activity, among which SAPO-34 showed superior catalytic performance compared to SAPO-18. DFT calculations were utilized to study the different catalytic performance of CHA and AEI. Significantly, SAPO-34 with the lowest silicon content, exhibited so far the longest catalyst lifetime and the lowest coking rate in MTO reaction than the reported catalysts tested under similar conditions. The straight 8-ring pore channel along *c* direction provided the optimum diffusion pathway as well as the shortest diffusion length for reactant and generated olefins, thus significantly reduced the coking rate. This work demonstrates that 3D EDT approach combined with TEM and EDS analysis from a single nanocrystal can provide clear crystal structure, crystal orientation and compositional information of nano crystals, which are useful for better understanding the catalytic performance of nanosized crystalline catalysts.

1 Introduction

Light olefins, such as ethylene and propylene, have been widely used as starting materials of polyolefins and as important raw materials for various chemicals in the petrochemical industry. However, the shortage of oil resources forces people to develop the preparation technology of light olefins that does not rely on oil resources.¹⁻³ Methanol-to-olefin (MTO) process has proven to be the most successful non-petrochemical route for the production of light olefins from the abundant resources of natural gas, coal, and biomass. Studies on MTO conversion have received extensive attention in the past decades.⁴⁻⁵

Because of the unique shape selectivity, microporous crystalline zeolites or molecular sieves with regular pore architectures have been widely applied in chemical industry as one of the most important solid catalysts.⁶⁻⁹ Up to now, a variety of zeolite materials have been tested as MTO catalysts, among which the aluminosilicate zeolite ZSM-5 with the zeotype MFI and the silicoaluminophosphate molecular sieve SAPO-34 with zeotype CHA are the most excellent catalysts for MTO

reactions.¹⁰⁻¹⁷ Compared with the ZSM-5, the selectivity towards light olefins is greatly improved by the application of SAPO-34 with large *cha* cage and small 8-ring pore opening. In general, SAPO-34 gives a very high selectivity (>80%) to light olefins (C₂-C₄) with 100% conversion of methanol.¹⁸ However, the main problem associated with the SAPO-34 catalyst is the rapid deactivation during methanol conversion because a large amount of organic species as retained materials accommodate in the large cavities connected by narrow channels.¹⁹ In order to suppress the catalyst deactivation and prolong the catalyst lifespan of SAPO-34 catalysts, various strategies have been developed to reduce the coke deposition, such as optimizing the operating conditions,^{12,20} modifying the catalyst acidity,²¹ decreasing the crystal size,¹⁹ and creation of secondary larger porosity,²²⁻²⁴ etc. Previous studies revealed that deactivation of catalysts in the MTO catalytic reactions mainly resulted from the restriction in mass transfer due to coke deposition, while the catalysts with small crystallite sizes showed their superiorities in the improvement of mass transfer and the reduction of coke formation.^{19,25} Chen et al. investigated the effect of selectivity and deactivation in the MTO reaction over SAPO-34 of different crystal sizes.¹⁹ The results showed that

the coking rate increased with increasing crystal size and SAPO-34 with the crystal size of less than 0.5 μm exhibited the longest lifetime in the MTO reaction. Similarly, Nishiyama et al. found that the smaller sized SAPO-34 showed longer catalysts lifetime and higher selectivity to light olefins than the larger sized counterpart.²⁶⁻²⁷ Recently, our group and others systematically investigated the size effect of SAPO-34 on the catalytic performance of MTO reactions.^{15, 18} Nanosized SAPO-34 crystals were synthesized by using microwave-assisted hydrothermal methods. The results demonstrated that the nanosized SAPO-34 catalysts exhibited remarkably enhanced MTO performance compared with those with ordinary crystallite size. Particularly, the nano sheet-like SAPO-34 of 20 nm in thickness gave the longest catalyst lifetime and the lowest coking rate in MTO reactions, which promises the potential application of nano SAPO-34 catalysts. However, the low product yield of ca. 15% of the nanosized SAPO-34 synthesized by microwave-assisted method limits their large-scale production. It is of importance to synthesize nanosized SAPO-34 with a high yield by using conventional hydrothermal synthesis method. In recent years, nano sheets-like zeolites have attracted extensive attention.²⁸⁻³² Particularly, significant enhancement of the reaction rate can be achieved with 2D zeolites having active sites on the surface because of a substantial increase in mass transfer.

On the other hand, the acidity of catalysts has a pronounced effect on the MTO catalytic performance. Dahl et al. emphasized that the acid-site density was the most important parameter for the deactivation and low acid-site density samples exhibited a longer lifetime than their high acid-site density analogues.³³ Recently, Zhu et al. found that less Si content in proton-type aluminosilicate zeolite SSZ-13 (CHA-type) resulted in a prolonged catalyst lifetime due to the reduced amount of Brønsted acid sites.³⁴ Thus, reducing the acidity by adjusting the Si/Al ratio of catalysts could decrease the rate of coking and prolong the catalytic lifetime of the catalysts.³⁵⁻³⁶ Several theoretical investigations were also reported in the literature to illuminate the mechanism and kinetics of silicon substitution in SAPO-34.^{35, 37} It is of highly interesting to synthesize nano SAPO-34 with decreasing Si contents to achieve better MTO catalytic performance.

Nevertheless, the nanosized crystalline catalysts often suffer from some problems, such as low crystallinity, impurity and crystalline defects due to the intergrowth of crystals, which will affect the catalytic performance of catalysts. As is well-known, both of SAPO-34 with the topological structure of CHA-type and SAPO-18 with the topological structure of AEI-type have similar double 6-ring (D6R) layers but in different stacking manners,³⁸ easily causing intergrowth during the crystallization, thus influence the catalytic performance. So it is necessary to investigate carefully the crystal structural features to better understand the catalytic performance of nanocrystals. However, the nano-scale dimensions of crystals bring difficulty into single-crystal structure determination using conventional X-ray technique, and powder X-ray diffraction only provides statistical data from the bulk of crystals. As compared to X-ray, electron has shorter wavelength and much stronger interaction with materials. A crystal needed for electron diffraction is around 10^{-8} times (area) smaller than that for single-crystal X-ray diffraction.

These advantages favor the function of electron diffractions in structural analysis of crystals, especially for nanosized crystals. Three-dimensional electron diffraction tomography (3D EDT) is a method to collect electron diffraction patterns slicing 3D reciprocal space, which is similar to single-crystal X-ray technique but uses electrons as a beam source.³⁹ During data collection, reciprocal space can be fine-scanned using the combination of a mechanical goniometer rotation and an electronic beam tilt at specified steps. This program-controlled technique requires neither alignment of crystals at low-index zone axes nor long data collection time. The partial 3D diffraction data collected from a randomly oriented crystal is free of principal zone axes in most cases which also decreases the dynamical scattering effects and improves the accuracy of electron diffraction intensities. By this method, reciprocal space with high resolution can be easily reconstructed; this opens new possibilities to study nanosized crystal structures in greater details.

In the present study, nano sheet-like SAPO-34 and SAPO-18 catalysts with different silicon contents were synthesized in a high product yield under conventional hydrothermal conditions using tetraethylammonium hydroxide (TEAOH) as the template. In order to understand the precise structures and catalytic performance of the synthesized nanocrystals, 3D EDT technique was applied for *ab initio* structure solution. Electron microscopy was used to certify the crystal orientation as well as the existence of defects. Our studies clearly demonstrate that reducing the silicon contents of nano sheet-like SAPO-34 can further prolong the catalytic lifetime in MTO reaction, and the SAPO-34 catalyst has longer catalytic lifetime and higher selectivity of light olefins (ethylene and propylene) than SAPO-18 catalyst. Particularly, SAPO-34 with the lowest silicon contents exhibited so far the longest catalyst lifetime and the lowest coking rate in MTO reaction than the reported catalysts tested under similar conditions. This work demonstrates 3D EDT technique combined with TEM and EDS analysis in a single nanocrystal can provide clear crystal structure, crystal orientation and compositional information of nanocrystals, which are of significance for better understanding the catalytic performance of nanosized crystalline catalysts.

2 Experiment section

2.1. Synthesis. The reagents used were aluminum iso-propoxide ($\text{Al}(\text{OPr})_3$, 99.5 wt%, Beijing Reagents Company), boehmite (Catapal B, 72.7% Al_2O_3 , Sasol), phosphoric acid (H_3PO_4 , 85 wt%, Beijing Chemical Works), tetraethylammonium hydroxide solution (TEAOH, 35 wt%, Alfa Aesar), colloidal silica (40 wt%, Aldrich).

The nano sheet-like SAPO crystals with different silicon contents were synthesized under conventional hydrothermal conditions from the starting gels with molar compositions of $1.0\text{Al}_2\text{O}_3 : 1.2\text{P}_2\text{O}_5 : 2.0\text{TEAOH} : x\text{SiO}_2 : 40\text{H}_2\text{O}$ ($x=0.6, 0.4, 0.2, 0.1$), and the resulting products were named as S1, S2, S3, and S4, respectively. Typically, the finely ground $\text{Al}(\text{OPr})_3$ was firstly mixed with TEAOH solution and deionized water at room temperature until dissolved completely. Phosphoric acid was then added dropwise to the resultant solution, followed by a continuous stirring for 2 h. Finally, colloidal silica was added

slowly. The reaction mixture was further stirred for 1 h, and was then transferred into a 100 mL Teflon-lined stainless steel autoclave. The crystallization was conducted in a conventional oven at 170 °C for 3 days under static conditions. The as-synthesized solid products were centrifuged, washed with water and ethanol for several times, and then dried at 80 °C in the oven overnight, followed by calcination at 550 °C for 6 h. The nano sheet-like SAPO-18 (named as S5) was prepared from a starting gel with the same molar composition as sample S3 except that the aluminium source was changed to boehmite.

2.2. Characterizations. The crystallinity and phase purity of the synthesized samples were characterized by powder X-ray diffraction with Bragg-Bretano configuration performed on a PANalytical X'Pert Pro using Cu tube equipped with monochromator (K α 1 radiation, 45 kV, 40 mA), irradiated length 15 mm, mask fixed 10 mm and a step size of 0.013°. Scanning electron microscope (SEM) images were recorded with a scanning electron microscopy using JEOL JSM-6510 and JSM-7401F. Chemical composition was determined with inductively coupled plasma (ICP) analyses carried out on a Perkin-Elmer Optima 3300 DV ICP instrument. Nitrogen adsorption/desorption measurement was carried out on a Micromeritics 2020 analyzer at 77.35 K after the sample was degassed at 350 °C under vacuum. The temperature-programmed desorption of ammonia (NH₃-TPD) experiments were performed on a Micromeritics Auto Chem II 2920 automated chemisorption analysis unit with a thermal conductivity detector (TCD) under helium flow. All NMR experiments were performed on a Varian Infinity-plus 400 spectrometer and Bruker AVANCE III 400 WB spectrometer operating at a magnetic field strength of 9.4 T. The resonance frequencies in this field strength were 161.9, 104.2, 79.5 and 400.1 MHz for ³¹P, ²⁷Al, ²⁹Si and ¹H respectively. ²⁹Si NMR experiments were carried out using a Chemagnetics 7.5 mm triple-resonance probe. A chemagnetics 5 mm triple-resonance MAS probe was employed to acquire ³¹P, ²⁷Al and ¹H NMR spectra. Magic angle spinning (MAS) rates were 4 kHz for ²⁹Si, 8 kHz for ³¹P and ²⁷Al, and 10 kHz for ¹H NMR experiments. ²⁹Si single pulse experiments were performed with a 4.5 μ s pulse width ($\pi/2$) and a 100 s recycle delay, and ¹H decoupling with radio frequency (RF) field strength of 38 kHz was applied during the acquisition period. The ²⁷Al MAS NMR spectra were acquired using a single pulse sequence with a short radio-frequency (rf) pulse of 0.5 μ s (corresponding to a $\pi/15$ flip angle) and a pulse delay of 1.0 s. The pulse length for ²⁷Al was measured using a 1 M Al(NO₃)₃ solution. Single-pulse ³¹P MAS NMR experiments with ¹H decoupling were performed with a 90° pulse width of 4.5 μ s, a 180 s recycle delay, and a ¹H decoupling strength of 42 kHz. The chemical shifts were referenced to a 85% H₃PO₄ solution for ³¹P, 1 M Al(NO₃)₃ solution for ²⁷Al, tetramethylsilane (TMS) for ²⁹Si and ¹H.

2.3. Structure analysis. 3D electron diffraction data sets were collected using *EDT-Collect* (Analitex) program⁴⁰ on a JEOL JEM-2100F microscope at 200 kV (Cs = 0.8 mm, point resolution = 1.9 Å) with Schottky-type field emission gun. The tilting angle for the crystal with phase **1** was from -44.2° to 49.3° at the step of 0.1° (total of 1020 frames). The tilting range for the crystal with phase **2** was from -29.7° to 49.6° at the step of 0.1° (total of 870 frames). The reconstruction of reciprocal space was done by the

EDT-Process program (Analitex)⁴⁰. The structures were solved by direct methods using *Sir* 2011.⁴¹ TEM images and selected area diffraction (SAED) patterns were collected on a JEOL JEM-4010 microscope at 400 kV (Cs=0.8mm, point resolution=1.5Å) with LaB₆ filament. Energy dispersive X-ray spectroscopy (EDS) analysis was done on a JEOL JEM-2100.

2.4. Density functional theory (DFT) calculations. Geometry optimizations were performed on acidic aluminosilicate-based cage clusters of H-CHA (36T) and H-AEI (36T) with the Gaussian 09 package at the ONIOM (B3LYP/6-31 G (d, p): AM1) level. The high DFT level was used for an embedded 3T-cluster, which includes one acid site, and the organic guest molecules. All of the dangling bonds were saturated by hydrogen atoms and the atoms were allowed to fully relax. The zero point energies were obtained at the ONIOM (B3LYP/6-31G (d, p): HF/6-31G (d)) level of theory. Dispersion was accounted for by means of D3 corrections as proposed by Grimme and co-workers.⁴² Frequency calculations were performed to identify the transition-states with only one imaginary vibrational frequency along the reaction coordinate. The intrinsic reaction coordinate (IRC) approach was followed by optimization of transition-state.

2.5. Catalytic test and carbon deposits analysis. Methanol conversion was performed in a quartz tubular fixed-bed reactor at atmospheric pressure. The catalyst (300 mg, 40-60 mesh) loaded in the quartz reactor (6 mm inner diameter) was activated at 500 °C in a N₂ flow of 30 mL/min for 1 h before starting each reaction run and then the temperature was adjusted to reaction temperature of 400 °C. The methanol was fed by passing the carrier gas (15 mL/min) through a saturator containing methanol at 40 °C, which gave a WHSV of 2.0 h⁻¹. The reaction products were analyzed using an on-line gas chromatograph (Agilent GC 7890N), equipped with a flame ionization detector (FID) and Plot-Q column (Agilent J&W GC Columns, HP-PLOT/Q 19091P-Q04, 30 m \times 320 μ m \times 20 μ m). The conversion and selectivity were calculated on CH₂ basis and dimethyl ether (DME) was considered as reactant in the calculation.

The amount of generated cokes in the nano SAPO catalysts after MTO reactions was determined by thermal analysis (TG) on a Perkin-Elmer TGA7 at a heating rate of 10 K min⁻¹ from room temperature to 800 °C under air flow.

3. Results and discussion

3.1. Crystallinity, morphology, and composition of nano SAPO crystals. Samples S1-S4 are obtained from the reaction gels with molar compositions of 1.0Al₂O₃: 1.2P₂O₅: 2.0TEAOH: xSiO₂: 40H₂O (x=0.6, 0.4, 0.2, 0.1) with different amount of SiO₂, while sample S5 is formed from the same starting gel as that for sample S3 except for changing the aluminium source. Fig 1 shows the powder XRD patterns of the synthesized nano SAPO samples. The XRD patterns of samples S1 and S2 are in agreement with that simulated from the CHA framework type, while the XRD patterns of S3 and S4 both reveal a mixture phase of the framework type of CHA and AEI.⁴³ It can be seen that CHA-type phase is predominant in S3, while AEI-type is the major phase in S4. The XRD pattern of sample S5 agrees with the simulated one from the AEI-type framework. The observed peak broadening indicates the nanoscale character of the as-synthesized SAPO samples.

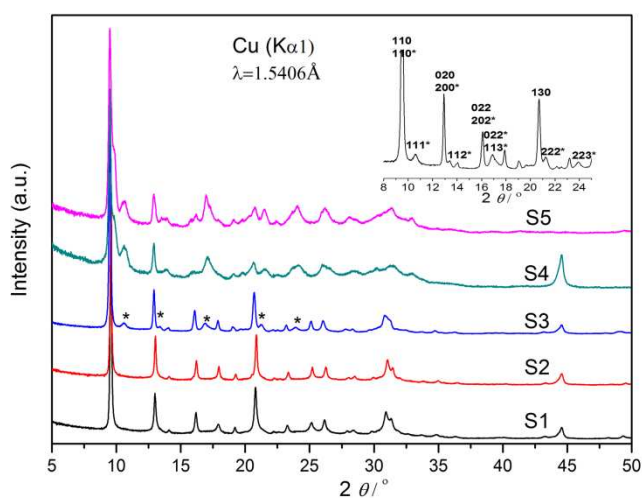


Fig. 1 Powder XRD patterns of as-synthesized nano SAPO crystals. S1: CHA-type; S2: CHA-type; S3: CHA-type/AEI-type; S4: CHA-type/AEI-type; S5: AEI-type. Asterisks denote reflections only from AEI-type. Range of 8°-25° of S3 is indexed (inset on the right top corner).

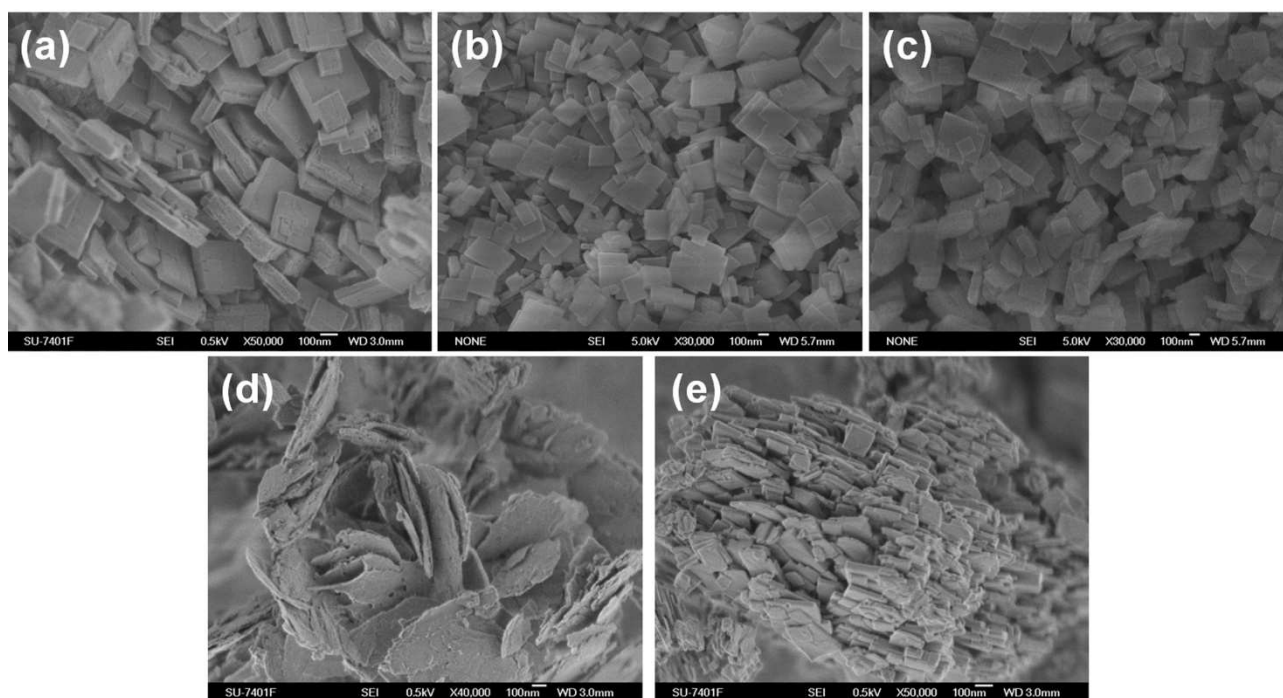


Fig. 2 SEM images of as-synthesized nano SAPO crystals. (a) S1; (b) S2; (c) S3; (d) S4; (e) S5. Scale bar in (a)-(e): 100 nm

3.2. 3D EDT structural analysis of nano SAPO crystals.

In order to understand the structural aspects and related them later to the catalyst performance, 3D EDT method has been used to collect electron diffraction data sets in 3D space. The structure analysis is mainly focused on the sample S3 with the best catalytic performance in MTO reaction that will be discussed in Section 3.4.

Several 3D EDT data sets are collected from the sample S3 which contains two phases uniquely identified by powder XRD analysis. All recorded electron diffraction frames are used for 3D reciprocal space reconstruction; corresponding reciprocal space volumes are shown in Fig 3 (phase 1) and Fig 4 (phase 2). The missing cone that can be seen in the 3D data is due to the

The SEM images of as-synthesized nano SAPO-samples are shown in Fig 2a-2e. It can be clearly seen that all of the crystals exhibit uniform nano sheet-like morphology. While, sample S4 exhibits much thinner sheet-like morphology than other samples.

In our previous studies, we obtained nanosized SAPO-34 with a similar morphology under microwave conditions, but with a rather low product yield of ca. 15%. In this work, all of the products have a very high yield up to 90%, which promises their future large-scale production.

The compositions of the nanosized SAPO samples determined by ICP are shown in Table 1. According to the chemical analysis, it can be seen that the silicon contents of the synthesized samples S1-S4 are decreased along with the decrease of silica added in the reaction mixtures. This will directly affect the acidic strength and concentration of the catalysts which will be discussed in later section. It should be noticed that the compositions of S3 and S4 are given based on a bulk mixture phase of CHA-type and AEI-type, but later TEM-EDS analysis will give the compositions of the individual nano crystals with CHA-type or AEI-type framework in the samples.

limitation of the goniometer tilting angles ($\pm 50^\circ$) and the beam stopper. Lattice constants and reflection indices are simultaneously determined from the analysis of reciprocal space data. As a result, two phases 1 and 2 are found with similar unit cell parameters: 1) $a=12.46\text{\AA}$; $b=13.48\text{\AA}$; $c=18.44\text{\AA}$; $\alpha=89.0^\circ$; $\beta=96.09^\circ$; $\gamma=90.33^\circ$ and 2) $a=13.53\text{\AA}$; $b=12.58\text{\AA}$; $c=18.38\text{\AA}$; $\alpha=90.24^\circ$; $\beta=90^\circ$; $\gamma=89.03^\circ$. Considering typical errors ($\sim 1-2\%$) in the unit cell parameters calculated from the EDT data, it is acceptable to set the angles of α and γ for phase 1 and α , β , γ for phase 2 to be 90° . Unlike X-ray, electrons interact with atoms strongly and dynamical scattering effects should be considered during the quantitative treatment of the experimental electron diffraction data. A crystal with higher symmetry requires less

tilting angle coverage in terms of the completeness of reciprocal space. Therefore, it is beneficial to take higher symmetry in the determination of Laue class necessary for the initial structure solution, especially in this case the lower symmetry only comes from distribution of different T atoms in the framework. The final symmetry would be carefully checked and lowered later during the refinement of atomic parameters against powder X-ray diffraction data. The Laue classes of the two phases are assumed to be $2/m$ and mmm , and the crystal systems to be monoclinic and orthorhombic, respectively. Combined with the absence conditions for hkl reflections (phase 1: hkl : $h+k=2n$; $h0l$: $h, l=2n$; $0k0$: $k=2n$; phase 2: hkl : $h+k=2n$; $h0l$: $h, l=2n$; $0kl$: $k=2n$), the space groups of the two phases are determined to be $C2/c$ (or Cc) and $Cmcm$ (or $Cmc2_1$). With all these conditions, both structures are consequently solved using direction methods in the *Sir2011* program. The structure solutions match well with the **CHA**-type and **AEI**-type frameworks for phases 1 and 2, respectively. The final refined structural modes for crystal with **CHA**-type (left) and **AEI**-type (right) phases are shown in Fig 5.

Diffuse streaks are also observed on electron diffraction patterns in 3D reciprocal space, indicating the existence of defects in the crystal structure. The slices cut from EDT data (Figure S1) reveal that streaks mainly appear along c^* on hkl ($k=0, \pm 1, \pm 2, \dots$) planes, implying the layer stacking faults along c axis and lateral shift along a axis on the basis of **CHA**-type framework. As is well known, the frameworks of **CHA**-type and **AEI**-type consist of identical D6R layers but stacking manners are different. The connectivity between two successive layers shows mirror symmetry in the **AEI**-type whereas translation symmetry in **CHA**-type (Figure S2).³⁸ The similarities of the two structures make it easy to form intergrowth during the crystal growth. As shown in Figs 6 and 7, TEM image presents that domains of **CHA**-type and **AEI**-type coexist in a single crystal. Except for this, the layers in both structures are connected by O atoms, which might be broken if charges of two connected D6Rs mismatch. In another sense, disorders would be arising from shift of D6R layers along a axis in **CHA**-type or b axis in **AEI**-type. This kind of stacking faults is also certified in TEM images (Fig 6c, d). However, it is worth mentioning that all diffractions on $00l$ are sharp, which means that layers are highly coherent along c direction. The powder XRD pattern refinement of sample S3 is conducted and the refinement result against a mixture of **CHA**- and **AEI**-type phases is shown in Figure S3, which gives a value of $R_p = 4.96\%$. The amount of **AEI**-type phase is estimated to be $\sim 30\%$. EDS analyses of **CHA**- and **AEI**-type framework single nanocrystals in the samples S1 to S5 are shown in Table 1. As with the bulk compositional analysis results by ICP, the Si contents in the individual **CHA**-type crystals of samples S1-S4 decrease along with the decrease of silica added in the reaction mixtures. The Si contents in the individual **AEI**-type nanocrystals of samples S3-S5 are increasing.

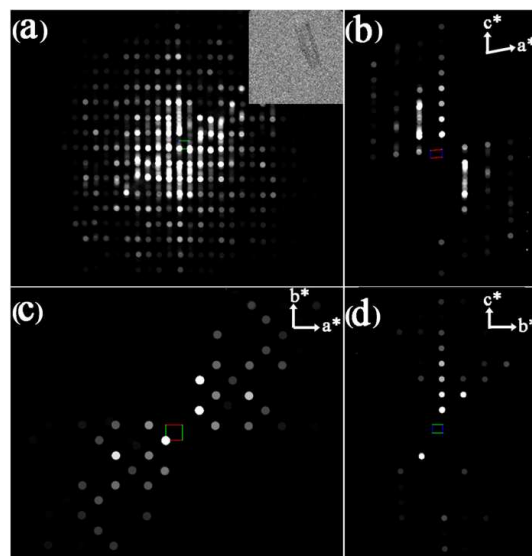


Fig. 3 Reconstructed 3D reciprocal space of phase 1. (a) The whole set of 3D EDT data (inset: the image of the crystal), (b) $h0l$ plane, (c) $hk0$ plane, and (d) $0kl$ plane cut from 3D reciprocal space.

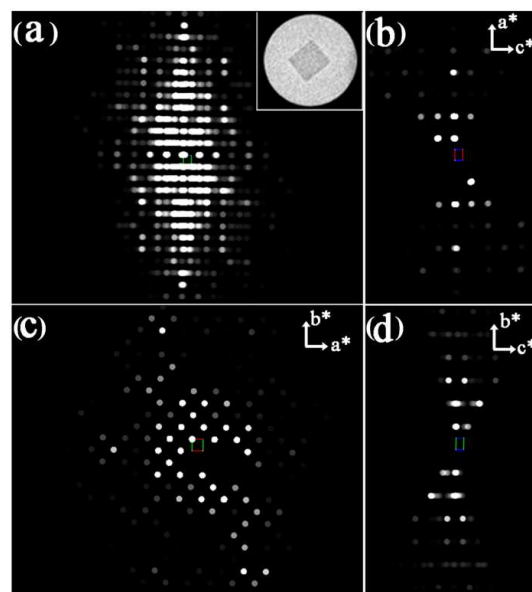


Fig. 4 Reconstructed 3D reciprocal space of phase 2. (a) The whole set of 3D EDT data (inset: the image of the crystal), (b) $h0l$ plane, (c) $hk0$ plane, and (d) $0kl$ plane cut from 3D reciprocal space.

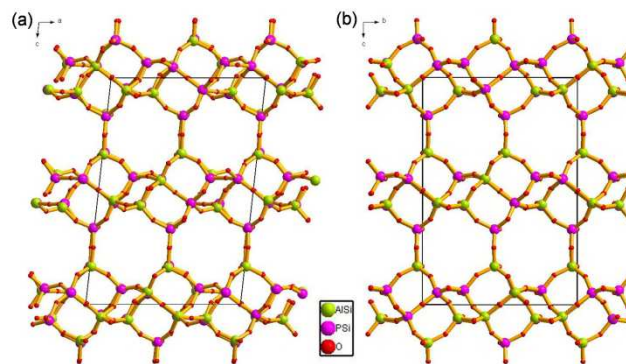


Fig. 5 Final refined structural models for crystals with (a) **CHA**-type and (b) **AEI**-type (O atoms from water are not included in the model).

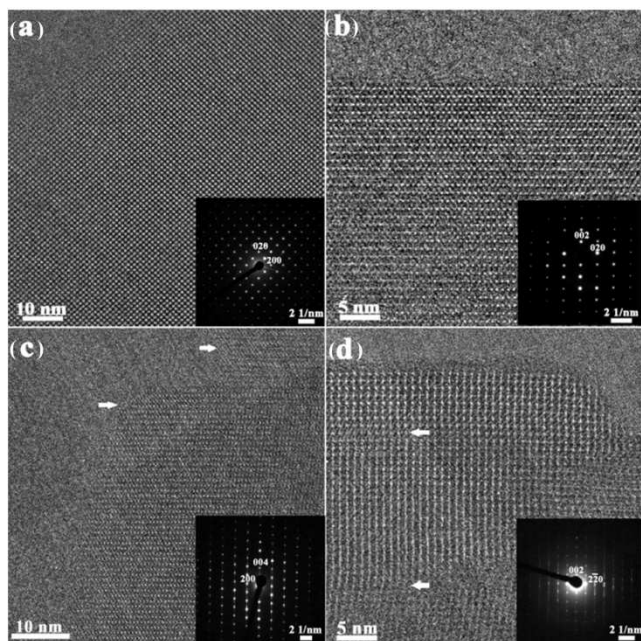


Fig. 6 HRTEM images and corresponding SAED patterns along (a) [001] (CHA-type /AEI-type), (b) [100] (AEI-type), (c) [010] (CHA-type) and (d) [110] (AEI-type & CHA-type) directions. The white arrows in c and d show the existence of defects.

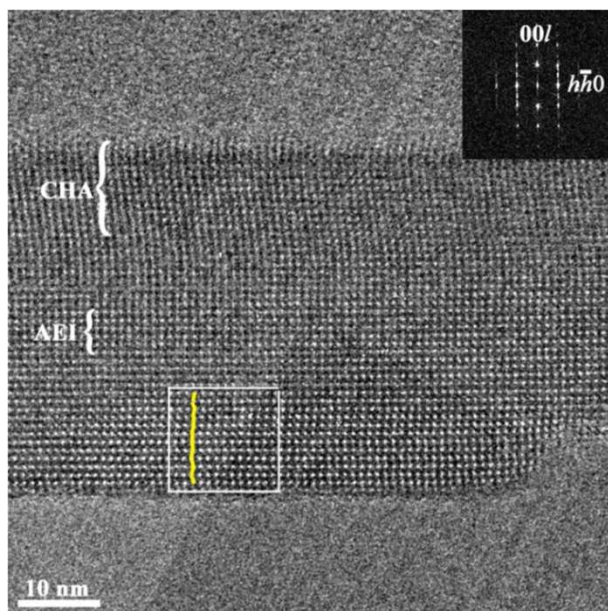


Fig. 7 TEM image of the S3 crystal with intergrowth of two types of framework. The inset on the top right corner is Fourier transformation of the area marked by the white square.

3.3 NH₃-TPD and texture properties of nano SAPO crystals.

The acidity of the calcined samples is evaluated by NH₃-TPD measurements and the profiles are shown in Fig 8. The desorption temperature indicates the acidic strength, whereas the peak area indicates the acidic concentration of the samples. All of the samples show two desorption peaks: the first peak in the range of 160–180 °C corresponds to weak acid sites, attributed to T–OH (T=Si, P, Al) hydroxyl groups; the second peak at high temperatures in the range of 380–410 °C, corresponds to the

20 strong acid sites.⁴⁴ As indicated in Figure 8, the strong acid strength of samples S1 to S5 is similar, while the concentration of strong acid sites decreases gradually with the decrease of the silicon contents in these nano SAPO samples.

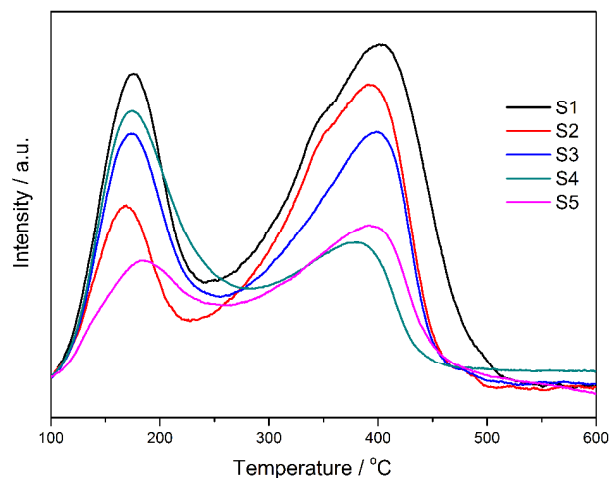


Fig. 8 NH₃-TPD profiles of as-synthesized nano SAPO crystals.

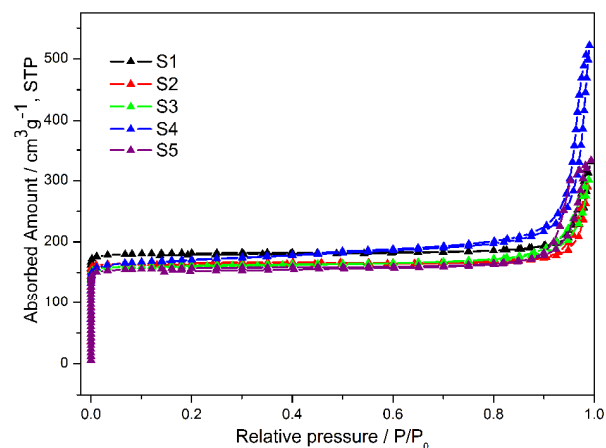


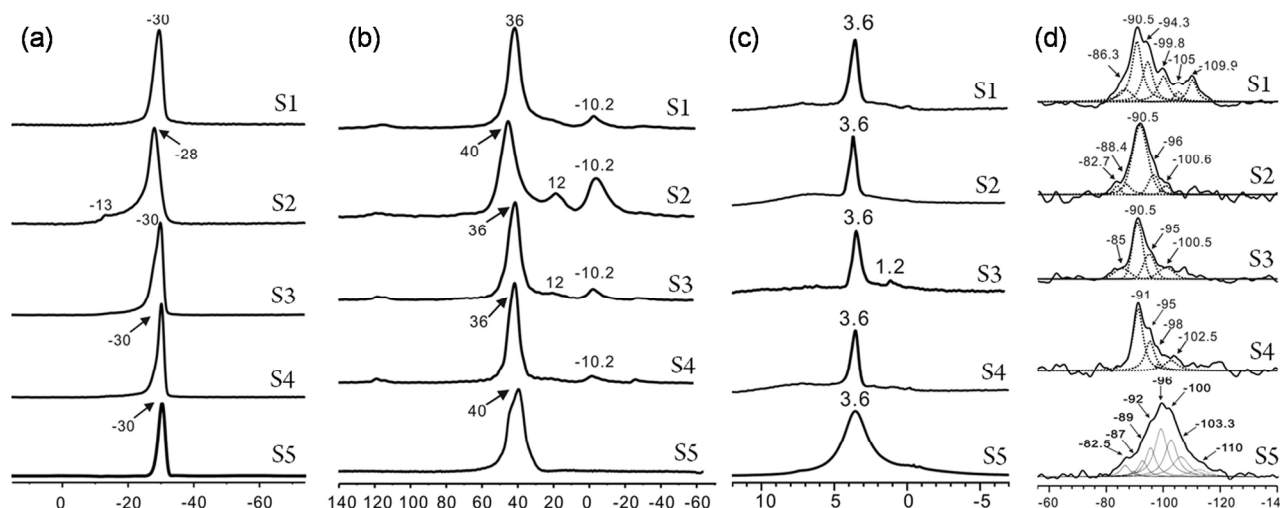
Fig. 9 N₂ adsorption/desorption isotherms of as-synthesized nano SAPO crystals.

30 The textural properties of calcined SAPO samples determined with N₂ adsorption/desorption measurements are shown in Fig 9 and summarized in Table 1. All isotherms display the characteristics Type I isotherms, confirming the microporosity of the samples. Meanwhile, the uptake near saturation pressure in the isotherms of samples is observed, due to the intercrystalline porosity typical of nano crystals. All of the samples show high surface areas (522.9–603.2 m²/g), with some variation in different samples. It can be seen that all of these samples possess some external surface, which is caused by some defects of the external surface as well as the intercrystalline porosity. Meanwhile, all of the samples have similar micropore volumes in the range of 0.23–0.27 cm³/g.

Table 1 Compositions and textural properties of the synthesized nano SAPO crystals

Sample No.	Phase identify	Molar Composition		$S_{\text{total}}(\text{m}^2/\text{g})^c$	$S_{\text{micro}}(\text{m}^2/\text{g})^d$	$S_{\text{ext}}(\text{m}^2/\text{g})^d$	$V_{\text{micro}}(\text{cm}^3/\text{g})^d$
		ICP ^a	Si/(Si+P+Al) ^b				
S1	CHA-type	Si _{0.20} Al _{0.43} P _{0.37} O ₂	0.17	603.2	580.6	22.5	0.27
S2	CHA-type	Si _{0.16} Al _{0.46} P _{0.38} O ₂	0.13	551.2	535.1	16.1	0.25
S3	CHA-type /AEI-type	Si _{0.14} Al _{0.48} P _{0.38} O ₂	0.08/0.04	537.9	505.6	32.3	0.24
S4	CHA-type /AEI-type	Si _{0.09} Al _{0.49} P _{0.42} O ₂	0.08/0.06	573.0	484.4	88.6	0.23
S5	AEI-type	Si _{0.12} Al _{0.48} P _{0.40} O ₂	0.10	522.9	491.7	31.2	0.23

^a Measured by inductively coupled plasma (ICP); ^b Measured by Energy Dispersive Spectrometer (EDS). ^c S_{BET} (total surface area) calculated by applying the BET equation using the linear part($0.05 < P/P_0 < 0.30$) of the adsorption isotherm; ^d S_{micro} (micropore area), S_{ext} (external surface area) and V_{micro} (micropore volume) calculated using the t-plot method.

**Figure 10.** (a) ³¹P, (b) ²⁷Al, (c) ¹H, and (d) ²⁹Si, MAS NMR (solid line) spectra of as-synthesized nano SAPO crystals.**Table 2** ²⁹Si MAS NMR deconvolution using Gaussian-Lorentzian function

Sample	S1	S2	S3	S4	S5
[Si(OAl) _n (OH) _{4-n}]	7.1%	11.8%	13.7%	0%	12.1%
Si(0Si4Al)	36.8%	71.0%	48.5%	49.5%	16.68
Si(1Si3Al)	23.1%	12.8%	23.3%	34.3%	25.0%
Si(2Si2Al)	16.4%	4.4%	14.5%	16.2%	26.1%
Si(nSi(4-n)Al) (n=3 or 4)	16.6%	0%	0%	0%	20.1%

3.3. Chemical environments of framework atoms measured by solid state MAS NMR. Fig 10 shows the solid-state ³¹P, ²⁷Al, ¹H, and ²⁹Si MAS NMR spectra of nano SAPO samples. All of the ³¹P MAS NMR spectra in Fig 10a show strong signals at ca. -30 ppm, resulting from tetrahedral phosphorus atoms in the coordination state of (P(OAl)₄).⁴⁵ A very weak peak appeared at -13 ppm implies the existence of a small amount of phosphorus atoms coordinated to water molecule in form of (P(OAl)₄(H₂O)).⁴⁵

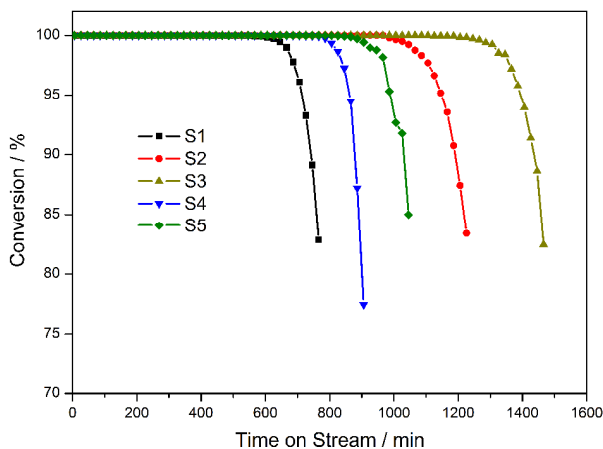
In the ²⁷Al MAS NMR spectra shown in Fig 10b, all of the samples give the strong peak at 36 ~ 40 ppm, due to the tetrahedral aluminum atoms.⁴⁶⁻⁴⁷ The weak signal at 12 ppm

indicates the presence of a small amount of pentacoordinated aluminum atoms formed by tetrahedral aluminum bonding one water molecular, while the weak peak at ca. -10 ppm is attributed to the octahedral aluminum atoms.⁴⁵

The ¹H MAS NMR spectra of dehydrated SAPO samples are shown in Fig 10c. The signals of bridging OH groups (SiOHAAl) appear at 3.6 ppm.⁴⁸ The weak signal at about 1.2 ppm is due to TOH (T=Si, P, and Al) groups of framework defects on the outer surface of the silicoaluminophosphate crystals.⁴⁸

Fig 10d shows the ²⁹Si MAS NMR spectra of the nano SAPO samples. The signals at ca. -91 ppm result from the Si(0Si4Al) unit. The peaks around -95 ppm and -100 ppm correspond to the signal of Si(1Si3Al) and Si(2Si2Al), respectively. The peaks below -100 ppm are ascribed to the Si(nSi(4-n)Al) (n=3 or 4) unit.⁴⁹ The other low-field shoulder signals are attributed to the Si(OAl)_n(OH)_{4-n} unit due to breaking of the Si-OH-Al bonds.⁵⁰ Table 2 gives the ratios of different Si states obtained from deconvolution of the ²⁹Si MAS NMR spectra using Gaussian-Lorentzian function. It can be seen that a relatively high amount of Si incorporated into S1 with the CHA phase results in the formation of Si islands, while decreasing the Si content in samples S2-S4 can efficiently avoid the formation of Si(3Si1Al) unit and silicon islands (Si(4Si0Al)). Meanwhile, S5 with the AEI phase exhibits diverse silicon species. According to the distributions of silicon coordination environments, the silicon

atoms incorporated into the AlPO_4 framework of all samples are enforced by the SM2 and SM3 substitution mechanism, while in S5 the SM3 mechanism appears predominant.⁵¹

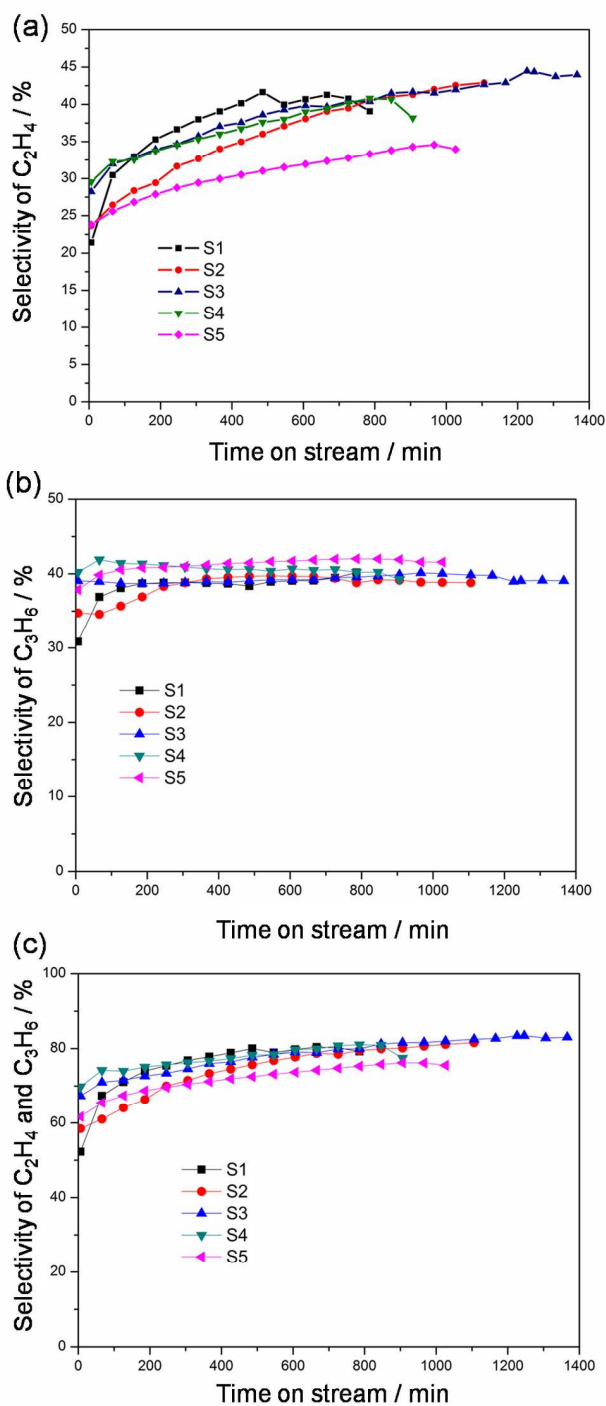


5 **Fig. 11** Methanol conversion variation with time-on-stream over nano SAPO catalysts with different silicon contents. Experimental conditions: WHSV = 2 h^{-1} , $T = 400 \text{ }^\circ\text{C}$, catalyst weight = 300mg.

3.4. Catalytic performance of nano SAPO catalysts in methanol conversion and DFT calculations.

Catalytic tests of methanol conversion were carried out at $400 \text{ }^\circ\text{C}$ in a fixed-bed reactor over the five nano sheet-like SAPO catalysts, and the results of conversion and selectivity of the products are given in Figures 11, 12 and Table S1. As shown in Fig 11, all these catalysts give a high initial catalytic activity with 100% conversion of methanol, while the catalyst lifespan, in which 100% methanol conversion can be kept and the occurrence of catalyst deactivation are different for samples S1~S5. All of the catalysts exhibit long catalyst lifetime and high catalytic activity because the nanosize of crystals can greatly enhance the mass transfer of reactant and generated products during methanol conversion as well as improve exposure of catalyst surface to the reactant. The deactivation occurs over samples S1 to S5 after time-on-stream of 606 min, 986 min, 1206 min, 686 min, and 866 min, respectively. Clearly, both silicon content and topological structure affect the catalytic lifetime. For samples S1 and S2 with **CHA** phase and S3 with **CHA**-type as the major phase, with the decrease of silicon contents, the catalyst lifetime turns to increase. This is because the decrease of acidic concentration can retard the coke formation and thus prolong the catalyst lifetime. While sample S4 with **AEI**-type as the major phase shows a different situation, even though it has the lowest acidic concentration among all samples, it does not possess the longest catalyst lifespan, which is connected with the relatively poor crystallinity as well as excessively low acidity that may not be suitable for catalytic reaction.⁵² Meanwhile, sample S5 with **AEI** phase exhibits the decreased catalytic lifetime compared to sample S2 with **CHA** phase. Significantly, the sample S3 with **CHA**-type as the major phase and the lowest silicon content as confirmed by TEM-EDS analysis exhibits so far the longest catalyst lifespan of 1206 min, which is much higher than that of 786 min for the nano sheet-like SAPO-34 catalyst as previously reported.¹⁸ This is because reducing the acidity of SAPO-34

catalysts could decrease the rate of coking and prolong the catalytic lifetime of the catalysts.³⁵⁻³⁶



45 **Fig. 12** Products distributions over nano SAPO catalysts with different silicon contents. Experimental conditions: WHSV = 2 h^{-1} , $T = 400 \text{ }^\circ\text{C}$, catalyst weight = 300 mg. (a) selectivity of C_2H_4 , (b) selectivity of C_3H_6 , and (c) selectivity of C_2H_4 and C_3H_6 .

50 Fig 12 shows the product distributions over the nano sheet-like SAPO catalysts. For all of the samples, the light olefins, such as ethylene and propylene are the main products in a total yield of 75.3% ~ 83.3%. The selectivity of all the generated products changes with time-on-stream. At the beginning period, the

selectivity of propylene is higher than ethylene, but with prolonging the reaction time, the selectivity of propylene changes slowly and even slightly decreases. In contrast, the selectivity of ethylene shows the continuous increase with time-on-stream due to the coke formation, which can lower activation energy of producing the ethylene and lead to the changes in the transition-state shape selectivity.⁴ Before the occurrence of the deactivation, the generated ethylene and propylene account for nearly 80% over samples S1 to S4, especially the selectivity of ethylene and propylene over sample S3 with the **CHA**-type as the major phase and possessing the lowest silicon content reaches up to 83.3%. However, compared with sample S3, the light olefin selectivity of sample S5 with **AEI** phase exhibits different situation. The selectivity of propylene over samples S3 and S5 is similar, while the selectivity of ethylene over sample S5 (33.3%) is evidently lower than that of S3 (42.5%). Clearly, SAPO-34 has superior catalytic selectivity towards ethylene and propylene compared to SAPO-18.

Table 3 The calculated catalytic reaction barrier energies for methylation and cracking ethylene and propylene in the cages of H-**CHA** and H-**AEI** catalysts based on hydrocarbon pool mechanism

E_{act} (kcal/mol)	H- CHA	H- AEI
Methylation	14.4	27.0
Cracking ethylene	55.1	63.9
Cracking propylene	32.1	55.4

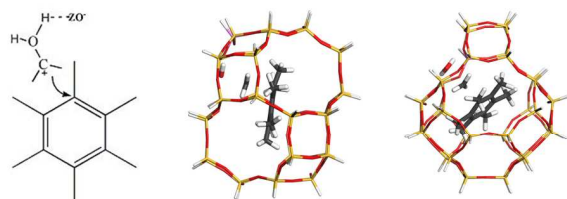


Fig. 13 Optimized geometries of transition-states for methylation from methanol on HMB using 36T cage clusters of H-**CHA** and H-**AEI** based on HP mechanism.

In order to understand the different selectivity between **CHA** and **AEI**, density functional theory (DFT) was employed to calculate the activation barriers for methylation and cracking ethylene and propylene using 36 T cage cluster model based on the hydrocarbon pool mechanism.⁵³⁻⁵⁴ The results of theoretical calculation are given in Fig 13 and Table 3. According to the calculation results, the geometries of transition-states of H-**CHA** and H-**AEI** are quite similar. However, H-**CHA** shows lower activation barriers for methylation (14.4 kcal/mol) than H-**AEI** (27 kcal/mol), indicating that H-**CHA** possesses higher catalytic activity in MTO conversion than H-**AEI**. In addition, the calculated reaction barrier energies for cracking ethylene and propylene are 55.1 kcal/mol and 32.1 kcal/mol for H-**CHA** and 63.9 kcal/mol and 55.4 kcal/mol for H-**AEI**, which indicates that propylene can be preferentially selected due to its lower-barrier than ethylene. Meanwhile, the catalytic reaction barrier energies for cracking ethylene and propylene in the cages of H-**AEI** catalyst are higher than H-**CHA**, which may lead to difficulty to produce ethylene and propylene over H-**AEI** as compared to H-

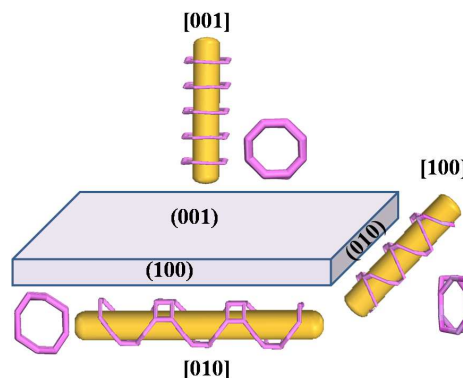
CHA. Particularly, the catalytic reaction energy barrier for cracking ethylene over H-**AEI** reaches up to 63.9 kcal/mol, which is much higher than that over H-**CHA**. This can explain why sample S5 with the **AEI** phase has more than 10% lower selectivity of ethylene than sample S3 with **CHA**-type as the major phase.

After reactions, all of the catalysts were dismantled and the coke formations over the deactivated catalysts were evaluated by thermal analysis (Table 4). The weight loss from the combustion of the retained coke species are 23.5%, 22.6%, 22.9%, 25.6%, and 23.2% for S1 to S5, respectively. Since the deactivation occurs at different time-on-stream, the amount of the coke deposited on the five catalysts corresponds to different duration of methanol conversion. In order to compare the coke formation over the catalysts, the average coking formation rate and the portion of reactant cost on coke generation were also evaluated taking account of the different time-on-streams and total feeding quality of methanol in the reaction. As illustrated in Table 4, samples S1 to S5 have a similar coke amount. However, the coking rate and the portion of methanol consumption on coke are different for these catalysts. Particularly, sample S3 shows the lowest coke formation rate of 0.057 mg/min, which ensures the best catalyst performance among all the samples.

Table 4. Variation of coke formation in methanol conversion over nano SAPO catalysts with different silicon contents.

Catalyst	S1	S2	S3	S4	S5
Coke (% , g/gcat)	23.5	22.6	22.9	25.6	23.2
R_{Coke} (mg/min) ^a	0.12	0.07	0.06	0.11	0.08
P_{Coke} (mg/g MeOH) ^b	11.6	6.9	5.7	11.2	8.0

^a R_{Coke} (mg/min) = coke amount (mg)/reaction time (min); ^b P_{Coke} (mg/g MeOH) = coke amount (mg)/methanol feedstock (g)



Scheme 1 Diffusion of methanol and generated products through 3D 8-ring channels along the [100], [010], and [001] direction of nano sheet-like SAPO-34 crystal.

The 3D EDT structure analysis combined with electron microscopy can give a nice explanation why SAPO-34 nano sheets can significantly enhance the mass transfer of reactant and generated products during methanol conversion. As is known, SAPO-34 framework consists of 3D 8-ring channels, which enable the diffusion of reactant and generated products during MTO conversion. As can be seen in Scheme 1, the straight 8-ring channel along the [001] direction may act as the optimum mass transfer pathway for methanol and generated olefins due to the

nearly parallel stacking of 8-rings. In contrast, the stacking of 8-rings along the [100] and [010] directions are fluctuant, thus reduce the effective diffusion. TEM observation reveals that the front face of nano sheet is (001) facet, which means that the shortest crystal dimension is along the [001] direction. Therefore, the nano sheets of SAPO-34 provide the optimum diffusion pathway as well as the shortest diffusion length for methanol and generated olefins, thus effectively reduce the coke formation rate.

4. Conclusions

In this work, nano sheet-like silicoaluminophosphate (SAPO) molecular sieves SAPO-34 (CHA-type) and SAPO-18 (AEI-type) with different silicon contents have been synthesized with a high product yield under conventional hydrothermal conditions by using tetraethylammonium hydroxide as the template. 3D EDT technique has been successfully applied to determine the CHA-type and AEI-type structures of synthesized nano crystals *ab initio*. Electron microscopy observations clearly reveal the crystal orientation, as well as the existence of intergrowth of CHA- and AEI-type frameworks due to different stacking manners of double 6-ring layers. The topological structure and the silicon contents of the as-synthesized nanosized SAPO catalysts have a pronounced effect on the catalytic performance in MTO reaction. With the decrease of silicon contents in SAPO-34, the catalyst lifetimes increase gradually, which is in accordance with the decrease of acidic concentration of the catalysts. Significantly, sample S3 with CHA-type as the major phase and the lowest silicon contents exhibits so far the longest catalyst lifetime (exceeding 1200 min) and the lowest coking rate in MTO reaction than other reported catalysts tested under the similar catalytic conditions. Moreover, sample S3 possesses the highest selectivity of ethylene and propylene reaching up to 83.3%. DFT calculations further explain the different catalytic performance between H-CHA and H-AEI, showing that H-CHA possesses higher selectivity towards light olefins than H-AEI. Furthermore, 3D EDT structure determine combined with TEM analysis explains the enhanced mass transfer of reactant and generated products during methanol conversion over SAPO-34 nano sheets. It shows that the nano sheets of SAPO-34 parallel to the (001) plane provide the optimum diffusion pathway as well as the shortest diffusion length for methanol and generated olefins along the [001] direction, thus effectively reduce the coke formation rate. This work provides a useful guidance for improving the methanol conversion process by utilizing nano crystalline, in particular, nano sheet-like silicoaluminophosphate catalysts. Moreover, it demonstrates the power of 3D EDT technique combined with TEM and EDS analysis in a single nanocrystal in providing clear crystal structure, crystal orientation and compositional information of nanocrystals. This is of significance for better understanding the catalytic performance of nanosized crystalline catalysts.

Acknowledgement

We thank the State Basic Research Project of China (Grant Nos. 2011CB808703 and 2014CB931802), National Natural Science Foundation of China (Grant Nos. 91122029 and 21320102001). Financial supports from VR (YM & PO), EXSELENT & 3DEM-

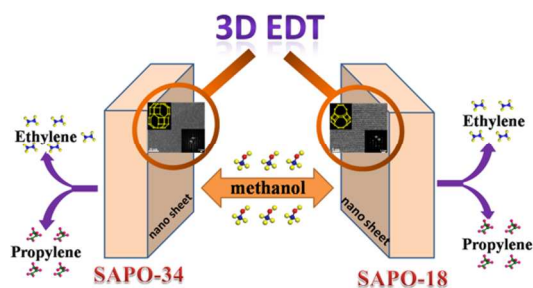
Natur (OT) Sweden and WCU/BK21Plus (OT) Korea are also acknowledged.

Notes and references

- ^a State Key Laboratory of Inorganic Synthesis and Preparative Chemistry, College of Chemistry, Jilin University, Changchun 130012, P. R. China. Tel: 86-431-8516-8608. Fax: 86-431-8516-8608. E-mail: jihong@jlu.edu.cn
- ^b Department of Materials & Environmental Chemistry, Stockholm University, S-10691 Stockholm, Sweden
- ^c Wuhan Center for Magnetic Resonance, State Key Laboratory of Magnetic Resonance and Atomic and Molecular Physics, Wuhan Institute of Physics and Mathematics, the Chinese Academy of Sciences, Wuhan 430071, P. R. China
- ^d Department of Chemistry, Sogang University, 35 Baekbeom-ro, Mapo-gu, Seoul, Korea
- ^e Department of Materials & Environmental Chemistry, Berzelii Centre EXSELENT on Porous Materials, Stockholm University, S-10691 Stockholm, Sweden
- ^f Graduate School of EEWS, BK21Plus, Korea Advanced Institute of Science and Technology, Daejeon 305-701, Republic of Korea
- ‡These authors contributed equally.
- † Electronic Supplementary Information (ESI) available: Slices cut from reconstructed reciprocal space of CHA-type phase, presentations for structural model of CHA-type framework and AEI-type framework, Rietveld refinement of powder XRD pattern of sample S3 and the detail MTO reaction catalytic results are provided as image. See DOI: 10.1039/b000000x/
1. C. D. Chang, A. J. Silvestri, *J. Catal.*, 1977, **47**, 249-259.
 2. C. D. Chang, *Catal. Rev.*, 1983, **25**, 1-118.
 3. C. D. Chang, *Catal. Rev.*, 1984, **26**, 323-345.
 4. D. Chen, K. Moljord, A. Holmen, *Micropor. Mesopor. Mater.*, 2012, **164**, 239-250.
 5. U. Olsbye, S. Svelle, M. Bjørgen, P. Beato, T. V. W. Janssens, F. Joensen, S. Bordiga, K. P. Lillerud, *Angew. Chem. Int. Ed.*, 2012, **51**, 5810-5831.
 6. Z. Wang, J. Yu, R. Xu, *Chem. Soc. Rev.*, 2012, **41**, 1729-1741.
 7. S. I. Zones, *Micropor. Mesopor. Mater.*, 2011, **144**, 1-8.
 8. A. Corma, *J. Catal.*, 2003, **216**, 298-312.
 9. Y. Li, J. Yu, *Chem. Rev.*, 2014, DOI: 10.1021/cr500010r.
 10. H. Yamazaki, H. Shima, H. Imai, T. Yokoi, T. Tatsumi, J. N. Kondo, *J. Phys. Chem. C.*, 2012, **116**, 24091-24097.
 11. H. Liu, L. Peng, N. Xue, X. Guo, W. Ding, W. Yang, Z. Xie, *App. Catal. A: Gen.*, 2012, **421-422**, 108-113.
 12. S. Lin, J. Li, R. Sharma, J. Yu, R. Xu, *Top. Catal.*, 2010, **53**, 1304-1310.
 13. S. Ilias, A. Bhan, *J. Catal.*, 2012, **290**, 186-192.
 14. W. Dai, M. Scheibe, L. Li, N. Guan, M. Hunger, *J. Phys. Chem. C.*, 2011, **116**, 2469-2476.
 15. Z. Li, J. Martinez-Triguero, P. Concepcion, J. Yu, A. Corma, *Phys. Chem. Chem. Phys.*, 2013, **15**, 14670-14680.
 16. H.-G. Jang, H.-K. Min, J. K. Lee, S. B. Hong, G. Seo, *App. Catal. A: Gen.*, 2012, **437-438**, 120-130.
 17. W. Dai, G. Wu, L. Li, N. Guan, M. Hunger, *Acc. Catal.*, 2013, **3**, 588-596.
 18. G. Yang, Y. Wei, S. Xu, J. Chen, J. Li, Z. Li, J. Yu, R. Xu, *J. Phys. Chem. C.*, 2013, **117**, 8214-8222.
 19. D. Chen, K. Moljord, T. Fuglerud, A. Holmen, *Micropor. Mesopor. Mater.*, 1999, **29**, 191-203.

20. S. Askari, R. Halladj, *Ultrason. Sonochem.*, 2012, **19**, 554-559.
21. M. Kang, T. Inui, *Catal. Lett.*, 1998, **53**, 171-176.
22. F. Schmidt, S. Paasch, E. Brunner, S. Kaskel, *Micropor. Mesopor. Mater.*, 2012, **164**, 214-221.
- 5 23. H. Yang, Z. Liu, H. Gao, Z. Xie, *J. Mater. Chem.*, 2010, **20**, 3227-3231.
24. Q. Sun, N. Wang, D. Xi, M. Yang, J. Yu, *Chem. Commun.*, 2014, **50**, 6502.
25. S. C. Larsen, *J. Phys. Chem. C.*, 2007, **111**, 18464-18474.
- 10 26. N. Nishiyama, M. Kawaguchi, Y. Hirota, D. Van Vu, Y. Egashira, K. Ueyama, *App. Catal. A: Gen.*, 2009, **362**, 193-199.
27. Y. Hirota, K. Murata, M. Miyamoto, Y. Egashira, N. Nishiyama, *Catal. Lett.*, 2010, **140**, 22-26.
28. W. J. Roth, J. Cejka, *Catal. Sci. Technol.*, 2011, **1**, 43-53.
- 15 29. W. J. Roth, P. Nachtigall, R. E. Morris, J. Čejka, *Chem. Rev.*, 2014, **114**, 4807-4837.
30. M. Choi, K. Na, J. Kim, Y. Sakamoto, T. Osamu, R. Ryoo, *Nature*, 2009, **461**, 246-250.
31. K. Na, C. Jo, J. Kim, K. Cho, J. Jung, Y. Seo, R. J. Messinger, B. F. Chmelka, R. Ryoo, *Science*, 2011, **333**, 328-332.
- 20 32. F. S. O. Ramos, M. K. d. Pietre, H. O. Pastore, *RSC Adv.*, 2013, **3**, 2084-2111.
33. I. M. Dahl, H. Mostad, D. Akporiaye, R. Wendelbo, *Micropor. Mesopor. Mater.*, 1999, **29**, 185-190.
- 25 34. Q. Zhu, J. N. Kondo, R. Ohnuma, Y. Kubota, M. Yamaguchi, T. Tatsumi, *Micropor. Mesopor. Mater.*, 2008, **112**, 153-161.
35. G. Sastre, D. W. Lewis, C. R. A. Catlow, *Acc. Chem. Res.*, 1997, **101**, 5249-5262.
36. A. Izadbakhsh, F. Farhadi, F. Khorasheh, S. Sahebdehfar, M. Asadi, Y. Z. Feng, *App. Catal. A: Gen.*, 2009, **364**, 48-56.
- 30 37. J. Tan, Z. Liu, X. Bao, X. Liu, X. Han, C. He, R. Zhai, *Micropor. Mesopor. Mater.*, 2002, **53**, 97-108.
38. C. Baerlocher, L. McCusker, <http://www.iza-structure.org/databases> 2012.
- 35 39. M. Gemmi, P. Oleynikov, *Z. Krist.*, 2013, **228**, 51-58.
40. <http://www.edt3d.com>.
41. M. C. Burla, R. Caliendo, M. Camalli, B. Carrozzini, G. L. Casciarano, C. Giacovazzo, M. Mallamo, A. Mazzone, G. Polidori, R. Spagna, *J. Appl. Cryst.*, 2012, **45**, 357.
- 40 42. S. Grimme, J. Antony, S. Ehrlich, H. Krieg, *J. Chem. Phys.*, 2010, **132**, 154104.
43. A. Simmen, L. B. McCusker, C. Baerlocher, W. M. Meier, *Zeolites*, 1991, **11**, 654-661.
44. T. Xiao, L. An, H. Wang, *App. Catal. A: Gen.*, 1995, **130**, 187-194.
- 45 45. C. S. Blackwell, R. L. Patton, *J. Phys. Chem.*, 1984, **88**, 6135-6139.
46. S. Ashtekar, S. V. V. Chilukuri, D. K. Chakrabarty, *J. Phys. Chem.*, 1994, **98**, 4878-4883.
47. A. M. Prakash, S. Unnikrishnan, *J. Chem. Soc., Faraday Trans.*, 1994, **90**, 2291-2296.
- 50 48. M. Hunger, *Catal. Rev.*, 1997, **39**, 345-393.
49. W. Shen, X. Li, Y. Wei, P. Tian, F. Deng, X. Han, X. Bao, *Micropor. Mesopor. Mater.*, 2012, **158**, 19-25.
50. M. Briend, R. Vomscheid, M. J. Peltre, P. P. Man, D. Barthomeuf, *J. Phys. Chem.*, 1995, **99**, 8270-8276.
- 55 51. G. Sastre, D. W. Lewis, C. R. A. Catlow, *J. Phys. Chem. B*, 1997, **101**, 5249-5262.
52. J. Chen, P. A. Wright, J. M. Thomas, S. Natarajan, L. Marchese, S. M. Bradley, G. Sankar, C. R. A. Catlow, P. L. Gai-Boyes, *J. Phys. Chem.*, 1994, **98**, 10216-10224.
- 60 53. J. F. Haw, W. Song, D. M. Marcus, J. B. Nicholas, *Acc. Chem. Res.*, 2003, **36**, 317-326.
54. K. De Wispelaere, K. Hemelsoet, M. Waroquier, V. Van Speybroeck, *J. Catal.*, 2013, **305**, 76-80.
- 65

Table of contents entry



3D EDT technique combined with TEM provides better understanding of the excellent MTO catalytic performance of nano sheet-like silicoaluminophosphate molecular sieves.